

The Fracture Behavior of 7085-T74 Al Alloy Ultra-Thick Plate During High Cycle Fatigue



PAN DAI, XIAN LUO, YANQING YANG, ZONGDE KOU, BIN HUANG, JINXIN ZANG, and JIGANG RU

As a new generation of Al-Zn-Mg-Cu alloy, 7085 Al alloy was first evaluated by high-cycle fatigue (HCF) tests. In the present work, HCF behaviors and the notch sensitivity of a 220-mm-thick 7085-T74 Al alloy ultra-thick plate were investigated. The fracture characteristics of the alloy were investigated, and the crack initiation mode of the alloy was proposed in the present study. The results show that the notch-sensitive coefficient is 0.367, which indicates that the 7085 Al alloy displays a sensitive notch effect. The fatigue crack initiation sites of 7085-T7452 Al alloy ultra-thick plate mainly occurred at the locations of coarse Fe-rich particles on the specimen surface. In addition, compared with smooth specimens, the notched specimens are prone to generating fatigue cracks and usually show more than one crack initiation site.

<https://doi.org/10.1007/s11661-020-05759-4>

© The Minerals, Metals & Materials Society and ASM International 2020

I. INTRODUCTION

THE lightweight 7000 series Al-Zn-Mg-Cu alloys are commonly used in the aeronautical industry because of its excellent properties of fracture toughness and strength.^[1-6] Among alloys of this series, 7085 Al alloy has attracted increasing interest because of its unique combination of low quenching sensitivity and good thermal stability after T74 treatment.^[7-10] In the last few years, 7085-T74 Al alloy ultra-thick plate has been mainly used in large structural components (such as the wings and tails) in advanced aircrafts, which are inevitably subjected to cyclic loading during the service.^[7,9] Therefore, higher requirements are demanded for the fatigue resistance of 7085Al alloy plate.

When used in aircraft as structural airframe parts, damage tolerance of the 7085-T74 Al alloy is an important parameter besides strength for the lifespans of aircraft wings and tails. Many investigations have been carried out on the fatigue properties of Al-Zn-Mg-Cu alloys.^[1,11-14] For example, De *et al.* evaluated the grain refinement on the fatigue life of 7075 Al alloy. Their results show that fine-grained 7075 Al alloy presents longer fatigue life than the parent 7075-T6 material.^[11] Wei *et al.* researched the fatigue behavior of

7050 Al alloy ultra-thick plate. They found that compared with 7050 Al alloy plate with less thickness, the ultra-thick plate shows an improved fatigue property due to the less densely populated particles.^[1] Nevertheless, in contrast to previous studies on 7075 and 7050 Al alloys, there is no open literature concerning 7085-T74 Al alloy ultra-thick plates. Furthermore, the 7085 Al alloy is often processed into parts with steps, corners, keyways, oil holes, *etc.*, which act as a notch effect and could change the stress state of the alloy and then cause stress concentration. Therefore, it is imperative to study the fatigue behavior and notch sensitivity of the commonly used 7085-T74 Al alloy ultra-thick plate under alternant load.

Hence, in the present work, high-cycle fatigue (HCF) tests were carried out on 7085-T7452 Al alloy ultra-thick plate. A crack initiation mode of the alloy was further proposed to describe the damage mechanism during fatigue testing.

II. EXPERIMENT PROCEDURE

The material used in this investigation was a 220-mm ultra-thick 7085-T7452 Al alloy plate with chemical composition (wt pct) of 7.56 Zn, 1.50 Mg, 1.45 Cu, 0.12 Zr, 0.06 Fe, 0.02 Si and balance Al. The fatigue tests were carried out on a MTS810 fatigue machine at ambient temperature according to the standard ASTM: E466-07. The tests were conducted at a frequency of 5 Hz under strain-controlled conditions ($R = \sigma_{\min}/\sigma_{\max} = 0.06$). The stress concentration factor is $K_t = 1$ (for smooth specimen) and $K_t = 3$ (for notched specimen). Specimens for microstructural observations

PAN DAI, XIAN LUO, YANQING YANG, ZONGDE KOU, and BIN HUANG are with the State Key Laboratory of Solidification Processing, Northwestern Polytechnical University, Xi'an 710072, P.R. China. Contact e-mails: luoxian@nwpu.edu.cn; yqyangnw@163.com JINXIN ZANG and JIGANG RU are with the Beijing Institute of Aeronautical Materials, Beijing 100095, P.R. China.

Manuscript submitted December 9, 2019.

Article published online April 19, 2020

and properties tests were taken from the 7085-T7452 thick plate (about 220 mm thick) in the position of 1/2 thickness along the longitudinal (L) direction. The tensile strength and yield strength of the alloy along L direction were 503 MPa and 462 MPa, respectively. The fracture surfaces of the failed specimens were examined by a field-emission FEI Nova 450 scanning electron microscopy (SEM) equipped with an Oxford Inca 350 X-ray energy dispersive spectrometer (EDS). The precipitate phases were characterized by a 300 kV FEI Tecnai F30 G^2 transmission electron microscopy (TEM).

III. RESULTS AND DISCUSSION

A. High-Cycle Fatigue Properties

Figures 1(a) and (b) shows the schematic of the smooth and notched specimens for the HCF test, respectively. Figure 1(c) shows the stress-life ($S-N$) curves of the smooth specimens ($K_t = 1$) and notched specimens ($K_t = 3$) of 7085-T74 Al alloy ultra-thick plate. For both the smooth and notched specimens, the fatigue life increases with the decrease of the stress amplitude. In particular, the number of cycles to failure exceeds 10^7 when the stress amplitudes of the smooth and notched specimens are 260 MPa and 150 MPa, respectively. Table I shows the notch-sensitive coefficient of the 7085-T74 Al alloy. The fatigue limit σ_r is determined by the staircase method. The notch-sensitive coefficient q can be calculated by the formula^[15,16]:

$$q = \frac{K_f - 1}{K_t - 1}, \quad [1]$$

with

$$K_f = \frac{\sigma_{r\text{-smooth}}}{\sigma_{r\text{-notch}}}, \quad [2]$$

where K_f is the fatigue notch coefficient, and $\sigma_{r\text{-smooth}}$ and $\sigma_{r\text{-notch}}$ are fatigue limits of the smooth specimen

and notched specimen, respectively. Table I shows that the fatigue limit of the smooth specimen (260 MPa) is about 56 pct of the yield strength (462 MPa), which is nearly twice that of the notched specimen. This implies that the existence of notch significantly decreases the fatigue limit of the 7085 Al alloy. The calculated notch-sensitive coefficient is 0.367, which indicates that the 7085 Al alloy displays a sensitive notch effect.

B. Fatigue Fracture Surface Morphology

The fatigue fracture surface characteristics of one smooth 7085-T74 ultra-thick Al alloy specimen are presented in Figure 2. Figure 2(a) shows the overall view of the crack surface morphology of the specimen. It can be seen that the fracture morphology of the specimen exhibits three distinctive fatigue regimes: (1) crack initiation, (2) crack propagation stage and (3) final fracture. The magnified image of the crack initiation regime (dashed blue oval) shown in Figure 2(b) indicates that the crack initiation sites mainly occurred on the specimen surface. The cracks propagated perpendicular to the L direction. Two particles (marked by 1 and 2 with red crosses) in the initiation regime were detected by EDS, and the results are listed in Table II. The data indicate that the particles are Fe-rich constituents. Therefore, in 7085-T74 Al alloy, Fe-rich constituents are the main sites for crack initiation, especially when they are located at a region of stress concentration. Moreover, several second cracks, uneven crystallographic planes and river patterns are the main features at the crack initiation. Clear fatigue striations can be observed under high magnifications in the stable crack propagation stage (Figures 2(c) and (d)), which were normally generated *via* a repeated plastic blunting-sharpening process because of the slip of dislocations in the plastic zone in front of the fatigue crack tip.^[8] In this work, the distance between the crack initiation site and the analyzed location is defined as d . The average spacing of adjacent fatigue striations is 90.23 nm when d is 0.7 mm (Figure 2(c)). Remarkable

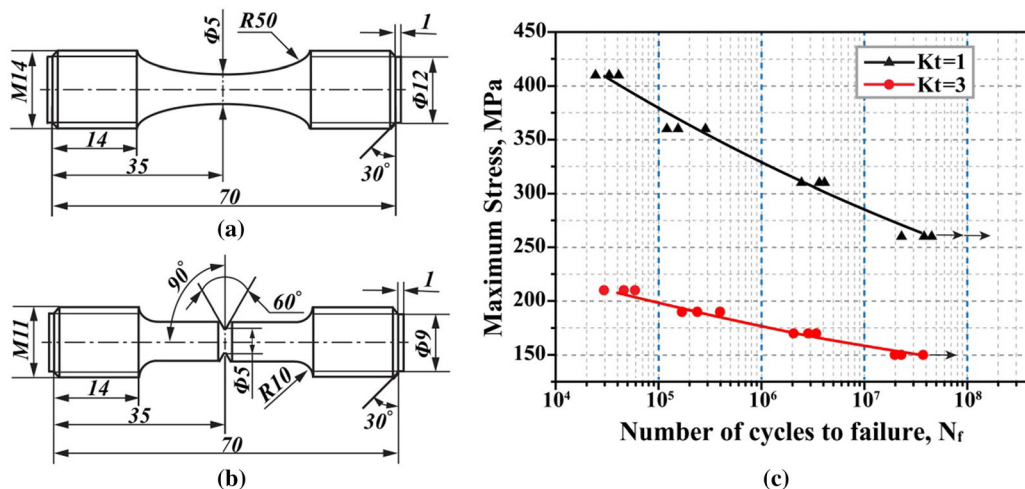


Fig. 1—Schematic of the HCF test specimens (dimensions in mm): (a) smooth specimen, (b) notched specimen and (c) $S-N$ curves of the 7085-T74 Al alloy ultra-thick plate.

differences of the neighbor fatigue striations spacing in grains with different orientations exist. The results revealed that the grain boundary can inhibit the propagation of fatigue crack. Moreover, Figure 2(d) shows that when d is 1.3 mm, the average spacing of adjacent fatigue striations increases to 556.74 nm. The final fracture morphology of the smooth specimen is shown in Figure 2(e). The yellow dashed and solid arrows indicate the intergranular cracks and dimples,

respectively. The white solid arrows indicate the voids. The fracture mode is the mixed rupture with transgranular fracture and intergranular fracture. A number of coarse particles are observed in the dimples, and some of them are broken into several parts. The EDS analysis result (at. pct: Al 67.37, Fe 32.63) in Figure 2(f) reveals that the particle is Fe-rich phase.

The fatigue fracture surface of one notched specimen is displayed in Figure 3. Figures 3(a) and (b) shows the overall view of the crack surface morphology and a higher magnification image of the crack initiation locations (blue dashed ovals) in Figure 3(a), respectively. The fracture morphology of the notched specimen also exhibits three distinctive fatigue regimes. Compared with the fracture characteristics of the smooth specimen (Figures 2(a) and (b)), there is more than one crack initiation site of notched specimens, also located at the specimen surface. The EDS results of the

Table I. Fatigue Limit and Notch-Sensitive Coefficient of the Smooth and Notched Specimens

Specimen	K_t	σ_r /MPa	q
Smooth	1	260	—
Notched	3	150	0.367

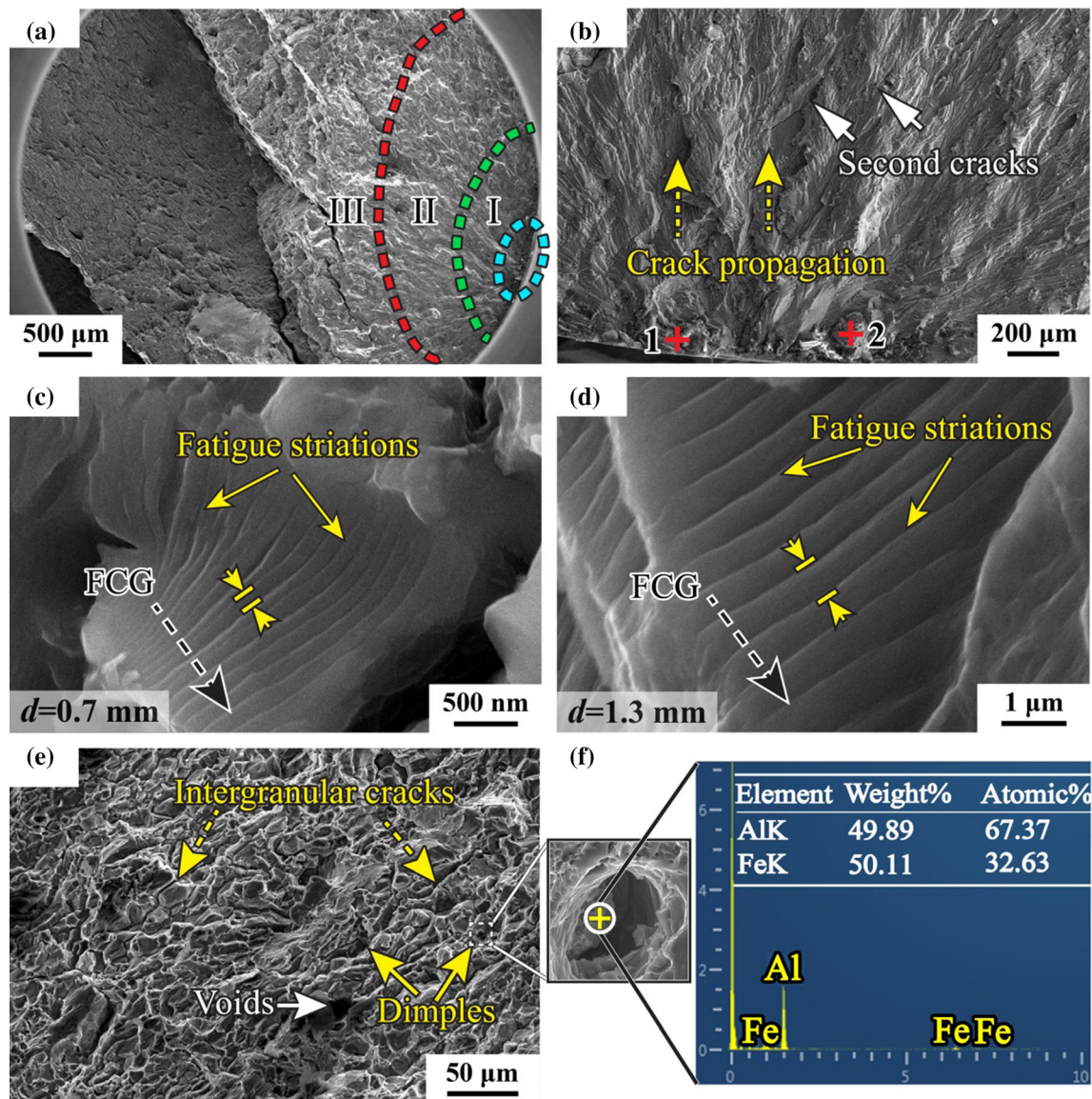


Fig. 2—Typical low-magnification secondary SEM images of the smooth specimen: (a) the fracture surface of the specimen, (b) fatigue crack initial stage, (c, d) regions of stable crack growth, (e) final fracture and (f) corresponding EDS result of the white circle (Color figure online).

particles (marked 3 and 4 with signs of red crosses) are listed in Table II. The data indicate that the particles are also Fe-rich constituents. Figures 3(c) and (d) shows that when d is 0.7 mm, the average spacing of adjacent

fatigue striations is 140.46 nm while the value achieves 361.27 nm when d is 1.3 mm. Figure 3(e) shows the final fracture morphology of the notched specimen, which also shows a mixed intergranular-transgranular fracture, but the intergranular mode becomes the dominant. The EDS analysis result (at. pct: Al 66.76, Fe 33.24) in Figure 3(f) reveals that the particle is also a Fe-rich constituent.

Table II. EDS Results of the Particles Marked with Red Crosses in Figs. 2(b) and 3(b)

Point Number	Weight Pct			Atomic Pct		
	Al	Fe	Cu	Al	Fe	Cu
1	53.33	13.71	32.96	72.12	8.96	18.92
2	56.24	14.28	29.48	74.34	9.12	16.54
3	50.92	11.92	37.16	70.28	7.95	21.77
4	57.56	14.91	27.53	75.29	9.42	15.29

C. Discussion

Compared with the smooth specimen, the notched specimen (Figure 1(b)) subjected to an applied cyclic fatigue load would generate an uneven distribution of stress and strain at the notch. Especially on the specimen surface, which is sensitive to fatigue, both the stress and strain would achieve peak values.^[17,18] This would easily lead to multiple positions at the top of the notch to meet

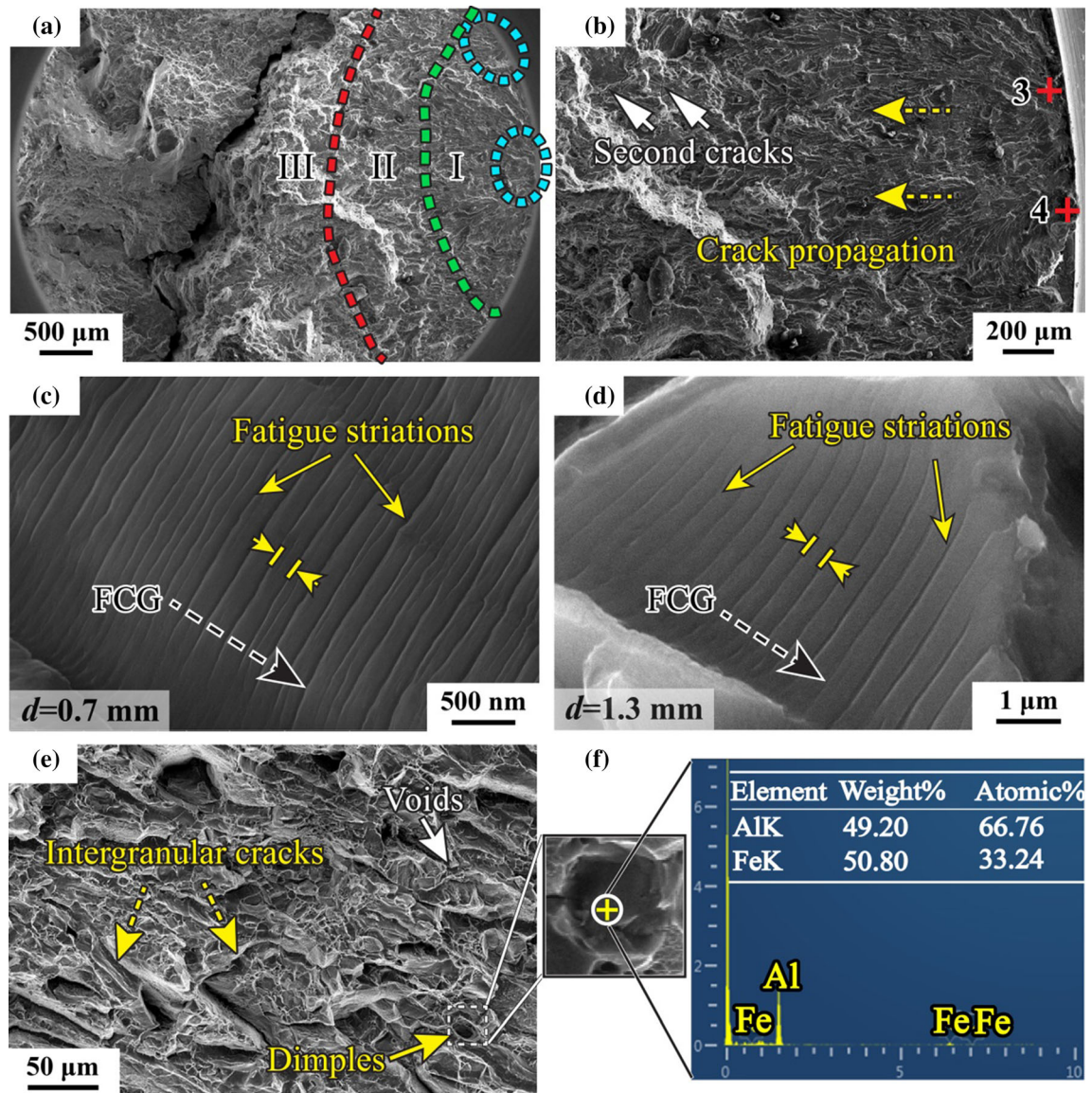


Fig. 3—Typical low-magnification secondary SEM images of the notched specimen: (a) the fracture surface of the specimen, (b) fatigue crack initial stage, (c, d) regions of stable crack growth, (e) final fracture and (f) corresponding EDS result of the white circle (Color figure online).

the requirement of crack initiation.^[19] Therefore, the notched specimen usually shows more than one crack initiation site.

Figure 4 displays the microstructure of the 7085-T7452 Al alloy ultra-thick plate. The microstructure of the alloy in Figure 4(a) contains elongated un-recrystallized grains and equiaxed recrystallized grains, indicating that partial recrystallization occurred in the alloy. The SEM backscattered electron image (Figure 4(b)) shows that many particles of 0.5 to 4 μm exist. The insert EDS result in Figure 4(b) shows that the particles are in the formation of $\text{Al}_7\text{Cu}_2\text{Fe}$ impurity phase. The SEAD pattern along the $[100]_{\text{Al}}$ zone axis in Figures 4(c) and (d) shows the enlarged SEAD pattern marked by the white dashed rectangle in (c). The results show the existence of Al_3Zr particles (orange arrows) and both η' and η phases (blue arrows). Previous studies proved that grain boundaries normally act as a blockage of crack growth and reduce the crack driving forces because of the energy induced by piled-up dislocations.^[13,20,21] As seen in Figure 4(e), the average width of the precipitate free zone (PFZ) is about 36.75 nm. Compared with the intragranular strength, the strength of the grain boundary is lower.^[7] This makes dislocation prone to preferentially slip at the soft PFZ, which leads

to the increase of stress concentration at the grain boundary. At the same time, the coarse η precipitates along the grain boundaries can also weaken the bonding strength between grains.^[9,22] As a result, the final fatigue fracture of the Al alloy contains many intergranular cracks (see Figures 2(e) and 3(e)).

In the initial stage of crack growth (stage I), the elastic stress concentration at the notch root acts as the driving force of crack growth. Once the crack length is larger than a certain size, the notch effect has no impact on fatigue crack growth. Therefore, in the following stage (stage II), at a similar number of cycles, the stress of the notched specimen is lower than that of the smooth one, which makes the driving force of the crack propagation decrease. The decrease of the crack propagation rate leads to a decrease of adjacent fatigue striation spacing (see Figures 2(d) and 3(d)).

Fracture observations in Figures 2(e) and 3(e) show that both the smooth and notched specimens contain dimples, intergranular cracks and voids in the final fracture region (stage III). The fatigue fracture mechanism of the alloy is a combination of microcracks and dimples. The fracture mode of the 7085 Al alloy is illustrated in Figure 5. Figure 5(a) shows the schematic of the fracture surface of the 7085-T74 Al alloy. On the

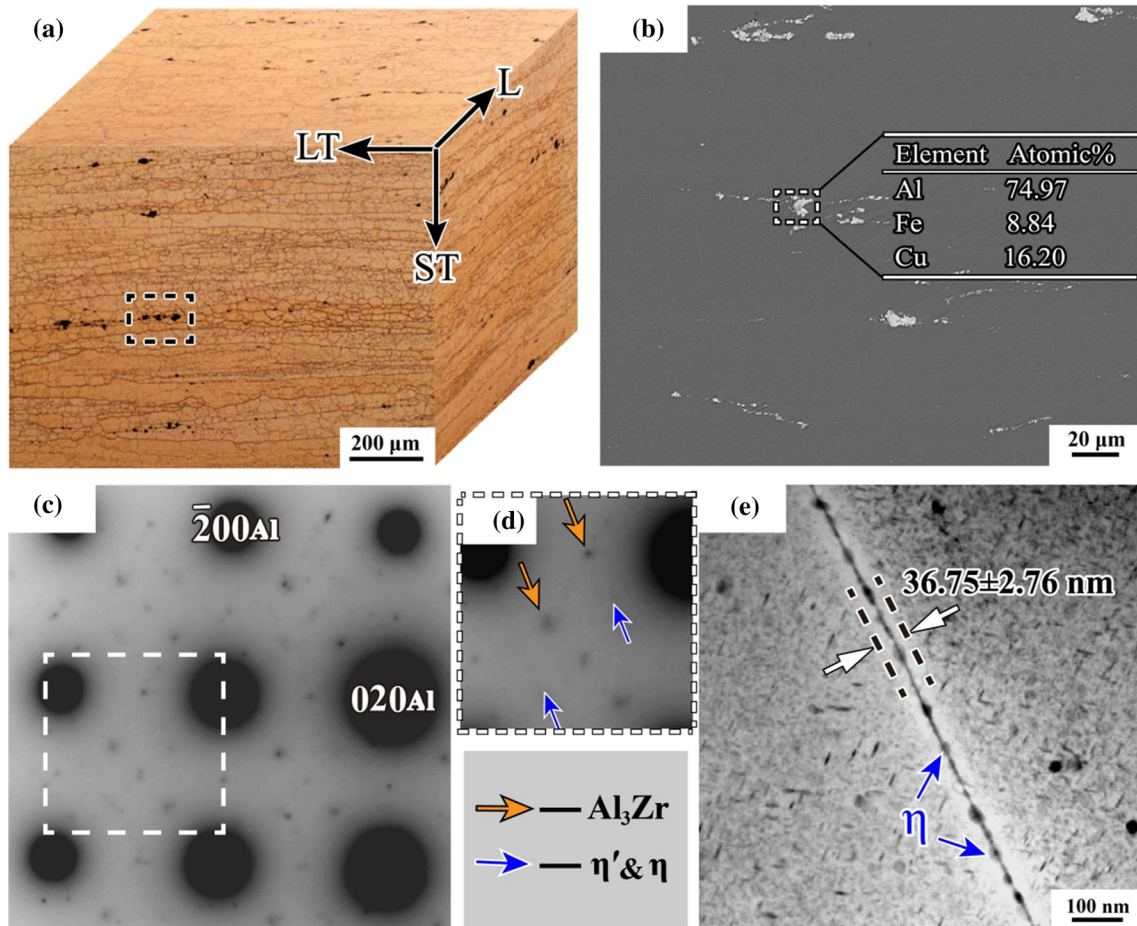


Fig. 4—Microstructure of the 7085-T7452 Al alloy ultra-thick plate: (a) optical microstructure, (b) SEM backscattered electron image, (c) SAED pattern along the $[001]_{\text{Al}}$ zone axis, (d) the enlarged SEAD pattern marked by the white dashed rectangle in (c) and (e) grain boundary (Color figure online).

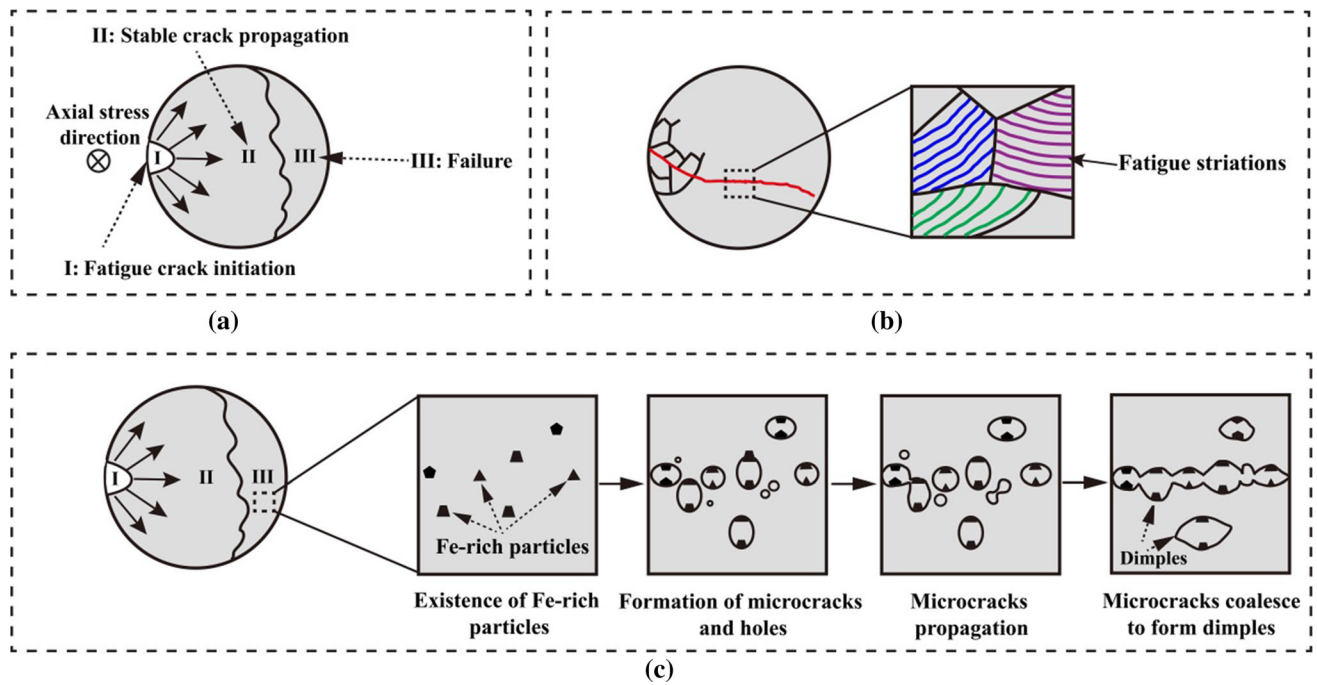


Fig. 5—(a) Fracture mode of the 7085 Al alloy ultra-thick plate, (b) formation of microcracks and (c) formation of dimples (Color figure online).

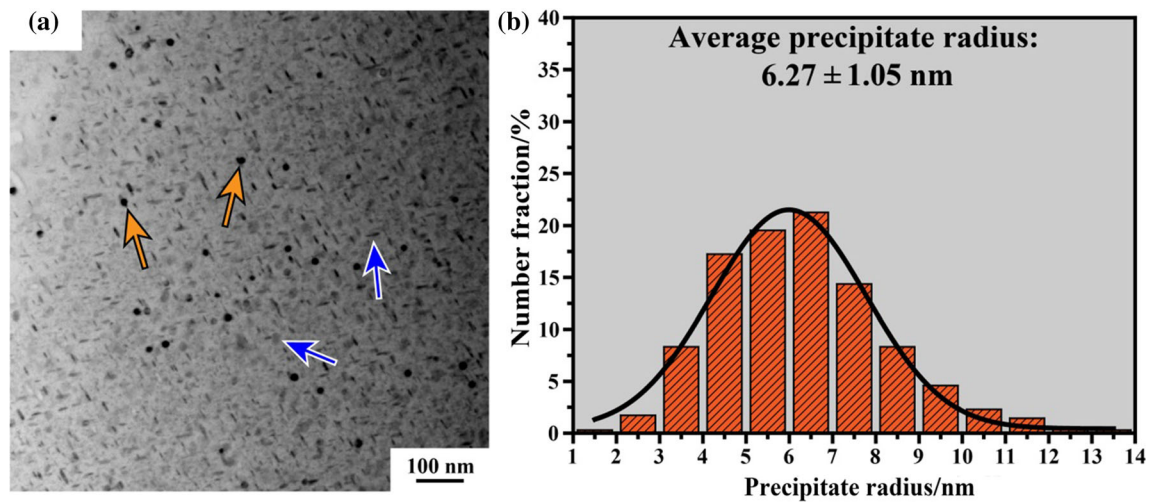


Fig. 6—(a) Bright field TEM image of precipitates in the grains and (b) precipitate size distribution (Color figure online).

one hand, for the formation of microcracks (Figure 5(b)), the microcracks initiate at the extrusion ridge and then propagate along the maximum shear stress direction. At the (I) stage, due to inhibition of grain boundaries, the microcrack propagation gradually turns in the vertical direction of tensile stress and comes into the (II) stage, characterized by transgranular propagation at room temperature. The characteristic of this stage is the formation of fatigue striations, which are the curved and parallel groove patterns. The fatigue striations are perpendicular to the fatigue crack

propagation. It is a microscopic trace left by crack growth, and each band can be regarded as an extension trace of a stress cycle.^[1]

Figure 6(a) shows the bright-field TEM image of precipitates in the grains, which indicates that the precipitates distributed homogeneously in the Al matrix. The resulting histogram of precipitate radius distribution is presented in Figure 6(b). The average precipitate size is 6.27 nm with a radius > 3 nm occupying almost 98 pct of the whole. Furthermore, the relationships between dislocations and precipitates (η' and η) analyzed

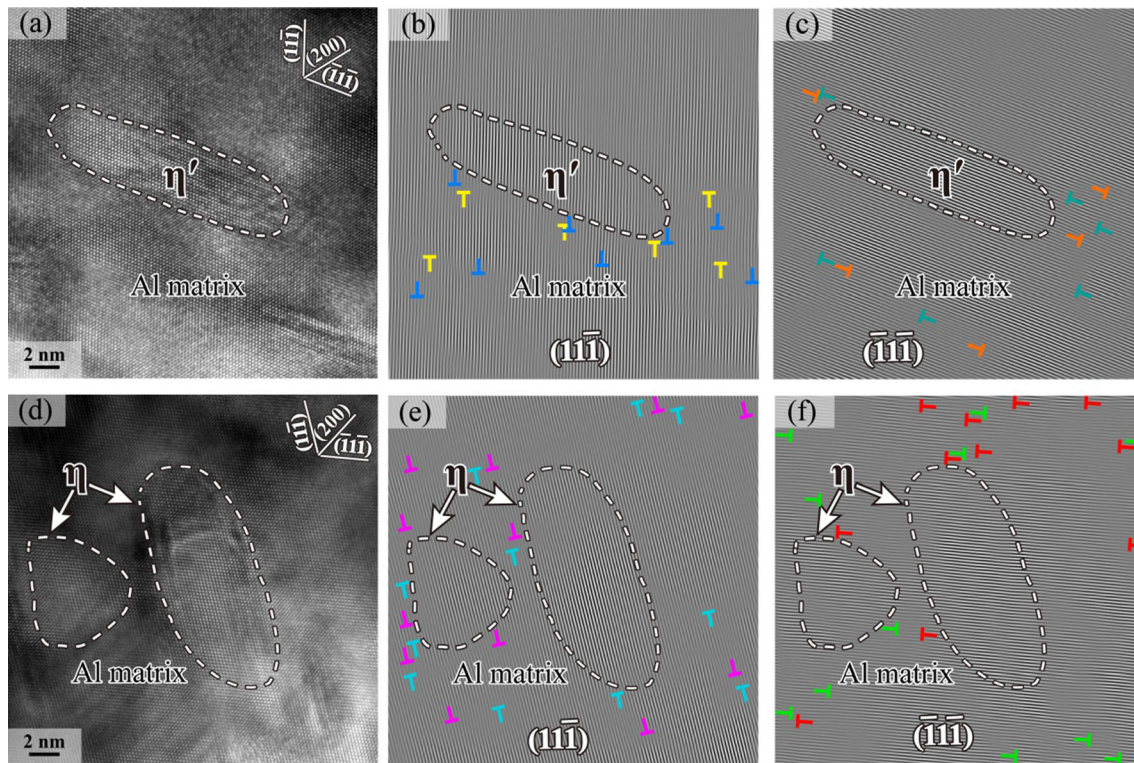


Fig. 7—(a) HRTEM image of η' precipitate, (b and c) corresponding inverse FFT patterns of (a), (d) HRTEM image of η precipitate and (e and f) corresponding inverse FFT patterns of (d).

by high-resolution transmission electron microscopy (HRTEM) images are shown in Figure 7. The plate-like η' phase with a radius of 4.6 nm in Figure 7(a) shows the base plane parallel to the habit planes $\{111\}_{\text{Al}}$. The corresponding inverse FFT images in Figures 7(b) and (c) indicate the dislocations distribute around the precipitates. Figure 7(d) shows the η' variants with disc-like and plate-like morphologies. Precipitates in the corresponding inverse FFT images (Figures 7(e) and (f)) surrounded by dislocations also indicate that the dislocations bypass the precipitates. Consequently, the irreversible plastic deformation is responsible for the fatigue crack propagation rates of the overaged 7085 Al alloy.^[23]

However, the fracture observations in Figures 2(f) and 3(f) also show that the small dimples evolve because of microcracks, which are mainly nucleated in the Fe-rich particles. As shown in Figure 5(c), under the cyclic fatigue load, the Fe-rich particles fracture, forming microcracks and holes. Then, the microcracks propagate and coalesce with each other in the Al matrix and eventually result in the dimples and tear ridges during the final fracture process.^[7,24] Dimples are the main microscopic characteristics of plastic fracture of metals.^[25–27]

The material has become an essential element of aircraft design in recent years. The present study measured the S-N curves of the commercial 7085-T74 ultra-thick plate for aviation. The results can provide the foundation for safety evaluation and design in industry. Moreover, the fatigue crack initiation behavior

and its mechanism were investigated to offer a reference for the fatigue damage mechanism of 7xxx series Al alloys. The nano-sized precipitate characteristics (precipitate size, type) and the relationship between dislocations and precipitates were investigated, which can provide a theoretical and experimental basis for the heat treatment of 7085 Al alloy.

In the aviation industry, the 7085 Al alloy plate is often processed into components with different notched types (steps, corners, keyways, oil holes, *etc.*), while the high stress concentration effect of notches can decrease the fatigue strength. In this study, the notch sensitivity is calculated to judge the stress concentration sensitivity of 7085 Al alloy. The result can also be used to determine the brittle fracture resistance of the Al alloys.

IV. CONCLUSIONS

In this study, the fatigue behavior and notch sensitivity of 7085-T74 Al alloy ultra-thick plate were first investigated. Through the analyses of experimental results and fatigue fracture observations, the main conclusions could be drawn as follows:

1. The fatigue crack initiation sites of 7085-T7452 Al alloy ultra-thick plate mainly appeared at the locations of coarse Fe-rich particles on the specimen surface.
2. The notch-sensitive coefficient is 0.367, which indicates the 7085 Al alloy has a sensitive notch effect.

3. Compared with smooth specimens, the notched specimen is prone to generating fatigue cracks and usually shows more than one crack initiation site.
4. The dislocations bypass both the nano-sized η' and η precipitates in the 7085-T74 Al alloy ultra-thick plate, which affect the fatigue crack propagation rates of the overaged 7085 Al alloy.

ACKNOWLEDGMENTS

The authors acknowledge the financial support of the Natural Science Foundation of China (Grant No. 51901184) and the Aviation Science Foundation of China (Grant No. 2016ZE53046).

REFERENCES

1. L.L. Wei, Q.L. Pan, Y.L. Wang, L. Feng, and H.F. Huang: *J. Mater. Eng. Perform.*, 2013, vol. 22, pp. 2665–71.
2. A. Singh, A. Pamakrishnan, and G.P. Dinda: *Metall. Mater. Trans. A*, 2019, vol. 50A, pp. 3949–58.
3. H. Masuda, H. Tobe, T. Hara, and E. Sato: *Scripta Mater.*, 2019, vol. 164, pp. 82–85.
4. A.M. Cassell, J.D. Robson, C.P. Race, A. Eggeman, T. Hashimoto, and M. Besel: *Acta Mater.*, 2019, vol. 169, pp. 135–46.
5. T.M. Ivanoff, J.T. Carter, L.G. Hector, Jr, and E.M. Taleff: *Metall. Mater. Trans. A*, 2019, vol. 50A, pp. 1545–61.
6. M.D. S. Bhuiyan, H. Toda, K. Shimizu, H. Su, K. Uesugi, A. Takeuchi, and Y. Watanabe: *Metall. Mater. Trans. A*, 2018, vol. 49A, pp. 5368–81.
7. P. Dai, X. Luo, Y.Q. Yang, Z.D. Kou, B. Huang, C. Wang, J.X. Zang, and J.G. Ru: *Mater. Sci. Eng. A*, 2018, vol. 729, pp. 411–22.
8. B.H. Nie, P.Y. Zhou, and T.T. Zhou: *Mater. Sci. Eng. A*, 2016, vol. 667, pp. 106–14.
9. P. Dai, X. Luo, Y.Q. Yang, Z.D. Kou, B. Huang, C. Wang, J.X. Zang, and J.G. Ru: *Mater. Charact.*, 2019, vol. 153, pp. 271–83.
10. Y.L. Zheng, C.B. Li, S.D. Liu, Y.L. Deng, and X.M.: *Trans. Nonferrous Met. Soc. China*, 2014, vol. 24, pp. 2275–81.
11. P.S. De, R.S. Mishra, and C.B. Smith: *Scripta Mater.*, 2009, vol. 60, pp. 500–03.
12. H.A. Elhadari, H.A. Patel, D.L. Chen, and W. Kasprzak: *Mater. Sci. Eng. A*, 2011, vol. 528, pp. 8128–38.
13. L. Chen, A. Yan, H.S. Liu, and X.Q. Li: *Trans. Nonferrous Met. Soc. China*, 2013, vol. 23, pp. 2817–25.
14. G. Rotella: *J. Manuf. Process.*, 2019, vol. 41, pp. 83–91.
15. Y.P. Zhao, J. Fang, and T.X. Yu: *Int. J. Ves. & Piping*, 1996, vol. 67, pp. 257–61.
16. L.W. Tsay, W.C. Lee, W.C. Luu, and J.K. Wu: *Corros. Sci.*, 2012, vol. 44, pp. 1311–27.
17. D.D. Tian, X.S. Liu, G.Q. He, Y. Shen, S.Q. Lv, and Q.G. Wang: *Mater. Sci. Eng. A*, 2016, vol. 654, pp. 60–68.
18. N. Eswara Prasad, D. Vogt, T. Bidlingmaier, A. Wanner, and E. Arzt: *Mater. Sci. Eng. A*, 2000, vol. 276, pp. 283–87.
19. T.S. Srivatsan, D. Kolar, and P. Magnussen: *Mater. Des.*, 2002, vol. 23, pp. 129–39.
20. Y. Xue, H.E. Kadiri, M.F. Horstemyer, J.B. Jordon, and H. Weiland: *Acta Mater.*, 2007, vol. 55, pp. 1975–84.
21. H.G. Jian, F. Jiang, K. Wen, L. Jiang, H.F. Huang, and L.L. Wei: *Trans. Nonferrous Met. Soc. China*, 2009, vol. 19, pp. 1031–36.
22. Y. Liu, D.M. Jiang, B.Q. Li, T. Ying, and J. Hu: *Mater. Des.*, 2014, vol. 60, pp. 116–24.
23. S. Bai, Z.Y. Liu, Y.X. Gu, X.W. Zhou, and S.M. Zeng: *Mater. Sci. Eng. A*, 2011, vol. 530, pp. 473–80.
24. C.D. Shao, H.C. Cui, F.G. Lu, and Z.G. Li: *Int. J. Fatigue*, 2019, vol. 123, pp. 238–47.
25. B.B. Guo, W.Z. Zhang, S.G. Li, and X.S. Wang: *Mater. Sci. Eng. A*, 2017, vol. 700, pp. 397–405.
26. M. Chemingui, M. Khitouni, K. Jozwiak, C. Mesmacque, and A. Kolsi: *Mater. Des.*, 2010, vol. 31, pp. 3134–39.
27. Z.C. Wu, S. Sandlöbes, L. Wu, W.P. Hu, and G. Gottstein: *Mater. Sci. Eng. A*, 2016, vol. 651, pp. 675–87.

Publisher's Note Springer Nature remains neutral with regard to jurisdictional claims in published maps and institutional affiliations.